Quantifying Star Formation Activity in the Inner 1 kpc of Local MIR Bright QSOs

M. Martínez-Paredes[1,2] , I. Aretxaga[3] , O. González-Martín[1], A. Alonso-Herrero[4], N. A. Levenson[5], C. Ramos Almeida[6,7], and E. López-Rodríguez[8]

[1] Instituto de Radioastronomía y Astrofísica UNAM Apartado Postal 3-72 (Xangari), 58089 Morelia, Michoacán, Mexico
[2] Korea Astronomy and Space Science Institute 776, Daedeokdae-ro, Yuseong-gu, Daejeon, 34055, Republic of Korea
[3] Instituto Nacional de Astrofísica, Óptica y Electrónica (INAOE), Luis Enrrique Erro 1, Sta. Ma. Tonantzintla, Puebla, Mexico; mariellauriga@kasi.re.kr, m.martinez@irya.unam.mx
[4] Centro de Astrobiología, CSIC-INTA, ESAC Campus, E-28692 Villanueva de la Cañada, Madrid, Spain
[5] Space Telescope Science Institute, Baltimore, MD 21218, USA
[6] Instituto de Astrofísica de Canarias (IAC), E-38205 La Laguna, Tenerife, Spain
[7] Departamento de Astrofísica, Universidad de La Laguna (ULL), E-38206 La Lagun, Tenerife, Spain
[8] Stratospheric Observatory For Infrared Astronomy (SOFIA), NASA Ames Research Center, CA 94041, USA

Abstract

We examine star formation activity in a distant ($z < 0.1$) and flux-limited sample of quasars (QSOs). Midinfrared (MIR) spectral diagnostics at high spatial resolution ($\sim$0.4 arcsec) yield star formation rates (SFRs) in the inner regions ($\sim$300 pc–1 kpc) for 13 of 20 of the sample members. We group these objects according to the size probed by the high angular resolution spectroscopy, with characteristic scales of <0.7 and $\sim$0.7–1 kpc. Using the polycyclic aromatic hydrocarbon (PAH) feature at 11.3 μm, we measure SFRs around 0.2 and 1.6 $M_\odot$ yr^{-1}. We also measure the larger aperture PAH-derived SFRs in the individual IRS/*Spitzer* spectra of the sample and obtain a clear detection in $\sim$58% of them. We compare smaller and larger aperture measurements and find that they are similar, suggesting that star formation activity in these QSOs is more centrally concentrated, with the inner region ($\lesssim$1 kpc) accounting for the majority of star formation measured on these scales, and that PAH molecules can be present in most local MIR-bright QSOs within a few hundred parsecs from the central engine. By comparison with merger simulations, we find that our estimation of the SFR and black hole (BH) accretion rates are consistent with a scenario in which the star formation activity is centrally peaked as predicted by simulations.

Key words: galaxies: star formation – infrared: galaxies – quasars: general

1. Introduction

An active galactic nucleus (AGN) harbors a supermassive black hole (SMBH, $M_{BH} \sim 10^6$–$10^9 M_\odot$), which is surrounded by an accretion disk responsible for the strong radiation field that ionizes the gas around it (e.g., Magorrian et al. 1998; Peterson & Wandel 2000; Gültekin et al. 2009; Du et al. 2015). Several studies have postulated that some of the gas in the vicinity of the AGN feeds the SMBH and fuels a central starburst located in comparable scales to a dusty torus (e.g., Cid Fernandes & Terlevich 1995; González Delgado et al. 1998; Wada & Norman 2002; Thompson et al. 2005; Ballantyne 2008; Diamond-Stanic & Rieke 2010; Feruglio et al. 2010; Miller et al. 2015). Indeed, there is observational evidence of nuclear (few hundred parsec scales) starbursts in several narrow-line AGNs, such as Seyfert 2 and low-ionization nuclear emission-line regions (LINERs), which have been detected through a variety of methods and wavelengths (e.g., Terlevich et al. 1992; Oliva et al. 1995; Colina et al. 1997; Heckman et al. 1997; González Delgado et al. 1998; Pović et al. 2016), and in Seyfert 1 galaxies (e.g., Imanishi & Wada 2004; Deo et al. 2006). Despite the large effort to understand how AGN activity influences the central star formation, this is still an open issue. Some studies have found a positive correlation between the star formation rate (SFR) and AGN luminosity (e.g., Netzer 2009; Esquej et al. 2014; Delvecchio et al. 2015; Gürkan et al. 2015; Matsuoka & Woo 2015; Dong & Wu 2016) while others have found none (e.g., Rosario et al. 2012; Azadi et al. 2015; Shimizu et al. 2015; Stanley et al. 2015). One explanation for this might be the different physical scales and AGN luminosities traced by the

various works, as well as finding good estimators of the SFR in AGNs.

Finding evidence of starbursts around type-1 AGNs has proven difficult, because the bright nucleus outshines classical starburst features, like the UV continuum emission and optical or near-infrared emission lines (e.g., Terlevich et al. 1990; Colina et al. 1997; Voit 1992; Cresci et al. 2004; Davies et al. 2007). Using IRS/*Spitzer* observations of Palomar–Green (PG) QSOs with a redshift $z < 0.5$, Shi et al. (2007) detected polycyclic aromatic hydrocarbons (PAHs) at 7.7 and 11.3 μm against the strong MIR AGN continuum on scales of $\sim$2–20 kpc. On the other hand, measuring the equivalent width (EW) of the PAH at 11.3 μm in the QUEST *Spitzer* survey, Schweitzer et al. (2008) found evidence for star formation in a sample of 27 PG QSOs at $z < 0.3$; 40% of objects showed clear PAH features, and for those that lacked individual detections the stacked spectrum revealed them, implying that starbursts are present in most QSOs at $\simeq$3.6 arcsec spatial resolution ($\sim$3–15 kpc).

There is a large variety of methods to estimate the SFR from PAHs (Farrah et al. 2007; Pope et al. 2008; Treyer et al. 2010; Diamond-Stanic & Rieke 2012), and the results could vary up to a factor of two according to the size of the sample and method used (Shipley et al. 2016). Shi et al. (2014) found a tight correlation between the SFR derived from the PAHs at 11.3 μm and the far-IR luminosity, suggesting that the PAH emission at 11.3 μm is a good indicator of the star formation activity in QSOs (see also, Netzer et al. 2007; Shi et al. 2007). Additionally, Shipley et al. (2016) calibrated the luminosity of the PAH features at 6.2, 7.7, and 11.3 μm as a measure of the

Table 1
Main Properties and Observational Details of the QSO Sample

Name	Group	z[a]	Angular Scale (kpc arcsec^{-1})	d (Mpc)	$L_{X(2-10\,\mathrm{keV})}$[b] (erg s^{-1})	Inner Physical Scale pc	Nuclear Spectrum[c]
PG 1501+106/MRK 841	1	0.0364	0.723	160	7.8×10^{43}	376	CC/GTC
MRK 509	1	0.0344	0.685	151	4.8×10^{44}	514	VISIR/VLT
PG 2130+099/IIZw136	1	0.0630	1.213	283	3.2×10^{43}	631	CC/GTC
PG 1229+204/MRK 771	1	0.0630	1.213	283	3.1×10^{43}	631	CC/GTC
PG 0844+349	1	0.0640	1.231	287	5.5×10^{43}	640	CC/GTC
MR 2251−178	1	0.0640	1.231	287	2.9×10^{44}	640	CC/GTC
PG 0003+199/MRK 335	1	0.0258	0.519	113	1.9×10^{43}	670	CC/GTC
PG 1440+356/MRK 478	2	0.0791	1.494	359	5.8×10^{43}	777	CC/GTC
PG 1211+143	2	0.0809	1.525	368	5.0×10^{43}	793	CC/GTC
PG 1426+015/MRK 1383	2	0.0866	1.622	395	1.3×10^{44}	843	CC/GTC
PG 1411+442	2	0.0896	1.627	397	2.5×10^{43}	846	CC/GTC
PG 0050+124/IZw1	2	0.0589	1.139	264	7.1×10^{43}	854	VISIR/VLT
PG 0804+761	2	0.1000	1.844	460	2.9×10^{44}	959	CC/GTC
PG 1448+273	⋯	0.0650	1.248	292	2.0×10^{43}	⋯	⋯
PG 1534+580	⋯	0.0296	0.593	130	1.8×10^{43}	⋯	⋯
PG 1535+547	⋯	0.0389	0.771	172	4.0×10^{42}	⋯	⋯
PG 2214+139	⋯	0.0658	1.263	296	6.6×10^{43}	⋯	⋯
PG 0923+129	⋯	0.0292	0.585	128	2.6×10^{43}	⋯	⋯
PG 1351+640	⋯	0.0882	1.649	403	1.2×10^{43}	⋯	⋯
PG 0007+106/MRK 1501	⋯	0.0893	1.667	408	1.4×10^{44}	⋯	⋯

Notes. Columns 1 and 2 give the name and assigned number group (defined in Section 3.2), columns 3, 4, and 5 show the redshift, angular scale, and distance, column 6 lists the intrinsic hard X-ray (2–10 keV) luminosity, and columns 7 and 8 list the inner physical scale, probed by the slit-width of the high angular resolution spectrum, and the instrument and telescope used to obtain the high angular resolution spectrum.
[a] NED.
[b] Zhou & Zhang (2010).
[c] Martínez-Paredes et al. (2017) and references therein.

SFR, and showed that the PAH SFR method is as accurate as those based on hydrogen recombination lines (i.e., H_α, Paα).

High angular resolution studies of nuclear (<100 pc) star formation in AGNs in the MIR are still scarce and limited to nearby Seyfert galaxies (e.g., Roche et al. 2006; Mason et al. 2007; Watabe et al. 2008; González-Martín et al. 2013; Alonso-Herrero et al. 2014; Esquej et al. 2014; Ramos Almeida et al. 2014; Ruschel-Dutra et al. 2017; Esparza-Arredondo et al. 2018). These studies showed that PAH emission in the nuclear region (few tens of parsecs) can be explained by the ionization produced by nuclear starbursts. Nevertheless, a recent study suggests that AGN excitation could also be an important component in heating/exciting PAH molecules in the nuclear region of active galaxies (Jensen et al. 2017).

Here we use MIR high angular resolution spectra to estimate, for the first time, the star formation activity within the central several hundred parsecs in local bright MIR QSOs using the PAH at 11.3 μm. We compare our results with merger simulations presented by Hopkins & Quataert (2010), which predict a relationship between the SFR, on a few parsecs and several tens of kiloparsecs, and the activity of the AGN. The paper is organized as follows: Section 2 describes the sample and observations; in Section 3 we present our measurements of the PAH feature; in Sections 4 and 5 we discuss our results; and in Section 6 we present the conclusions. Throughout this paper we have assumed the following cosmology: $H_0 = 70$ km s^{-1} Mpc^{-1}, $\Omega_m = 0.3$, and $\Omega_\Lambda = 0.7$.

2. Sample and Observations

We use the sample of Martínez-Paredes et al. (2017), which was built according to the following criteria: (1) a redshift $z < 0.1$ in order to study the inner MIR emission at scales $\lesssim 1$ kpc; (2) an N-band flux $f_N \geqslant 0.02$ Jy in order to detect these objects from the ground; and (3) a hard X-ray luminosity $L_{2-10\,\mathrm{keV}} > 10^{43}$ erg s^{-1} as an indicator of intrinsic powerful AGN activity. This sample of 20 AGNs is representative of nearby, MIR-bright quasars.

These data enable us to study the inner (few hundred parsecs) MIR emission of the PAH at 11.3 μm in QSOs, that is directly associated with recent star formation. Table 1 lists basic galaxy properties of the sample.

2.1. Inner ($\lesssim$1 kpc) N Band Spectra

We have inner ($\lesssim 1$ kpc) spectra in the N band (~ 7.5–13.5 μm, rest-frame wavelength) of 13 QSOs. Eleven of these were obtained with the MIR instrument CC on GTC as part of the ESO-GTC program (P.I: A. Alonso-Herrero, ID program: 182.B-2005, Alonso-Herrero et al. 2016a), guaranteed time (P.I: C. Packham, Packham et al. 2005) program, and Mexican open time (P.I.: I. Aretxaga/M. Martínez-Paredes). The spectra were obtained with a slit-width of 0.52 arcsec in low resolution mode ($R = 175$). The data were reduced using the pipeline for CanariCam developed by González-Martín et al. (2013). For more details on the observations and data reduction please refer to Martínez-Paredes et al. (2017) and Alonso-Herrero et al. (2016a, 2016b).

Two of the MIR spectra were obtained with VISIR on the VLT, MRK 509 (Hönig et al. 2010) and PG 0050+124 (Burtscher et al. 2013). These spectra were obtained in low spectral resolution mode ($R \sim 300$), with a slit-width of 0.75 arcsec and angular resolution $\sim$0.3 arcsec.

2.2. IRS/Spitzer Spectra (≲6 kpc)

We obtained the reduced 2D low resolution ($R \sim 60$–127) IRS/Spitzer spectra (Schweitzer et al. 2006; Shi et al. 2007) for all 19 QSOs available in the CASSIS database (v6., Lebouteiller et al. 2011). MR 2251−178 does not have a Spitzer spectrum. The spectra include the SL1 ($\lambda \sim 7.4$–14.5 μm) and SL2 ($\lambda \sim 5.2$–7.7 μm) modules acquired with a slit-width of 3.6 arcsec, and the LL1 ($\lambda \sim 19.9$–39.9μm) and LL2 ($\lambda \sim 13.9$–21.3 μm) modules acquired with a slit-width of 10.5 arcsec (Houck et al. 2004; Werner et al. 2004). We built stitched spectra between 5–35 μm by scaling the flux of the LL and SL1 modules in the overlapping wavelengths of module SL2. The scaling factors were around 1.1 (Martínez-Paredes et al. 2017).

3. Measuring the PAH Feature at 11.3 μm

There are a variety of methods and tools to measure the PAH features (e.g., Uchida et al. 2000; Peeters et al. 2002; Smith et al. 2007; Mullaney et al. 2011; Xie et al. 2018). However, they are limited to spectra having a large spectral range and clear PAH features. Hernán-Caballero & Hatziminaoglou (2011) presented a method that implements a linear interpolation to fit a local continuum between two narrow bands on both sides of the PAH feature and integrates the area between the local continuum and spectral feature. This method allows us to measure the PAH features reliably, especially in objects with weak PAH features observed over narrow spectral ranges (Esquej et al. 2014).

3.1. The Inner and Larger Aperture Nuclear Spectra

We measure the flux and EW of the PAH at 11.3 μm ($f_{11.3\ \mu m}$, EW$_{11.3\ \mu m}$) for the CC and VISIR spectra of each QSO. In order to do this, we first generate fiducial mean values of each continuum band by bootstrapping on the measured fluxes (hatched pink regions in Figure 1). We generate 100 continuum values for the two continuum bands, taking into account the uncertainties of the spectrum. We randomly associate shorter and longer wavelength mean continuum values to generate linear continua below the PAH feature. Next, to measure the flux we integrate the continuum-subtracted spectrum between the continuum bands. Then, we divide the integrated flux by the flux of the local continuum at 11.3 μm to calculate the EW$_{11.3\ \mu m}$. The continuum bandwidths are in the range $\Delta_{\lambda 1} = 10.6$–11.0 μm and $\Delta_{\lambda 2} = 11.4$–11.7 μm. The uncertainties are estimated repeating this process 100 times as shown in Figure 1. The values reported in Table 2 are the mean and standard deviations.

In order to determine if the PAH is clearly detected, we measure the variation of the continuum on both sidebands of the PAH feature, and use it as the level of noise. Then, comparing the flux of the PAH at 11.3 μm with the level of noise we find that for five objects the feature is clearly detected with a signal above 3σ. For PG 0804+761 and PG 1211+143, the PAH is also detected with a signal above 3σ. However, the large errors in the spectra, due to the marginal weather conditions during the observations (precipitable water vapor $\sim$8 mm, Martínez-Paredes et al. 2017), do not allow us to clearly see the PAH above the continuum (see panel (c) in Figure 1), and hence we report upper limits. For the other six objects, we also report upper limits (see Table 2).

In order to make a proper comparison between the results obtained from the PAH at 11.3 μm on the CC and VISIR and the IRS/Spitzer spectra, we follow the same method previously described to measure the flux and EW of the PAH at 11.3 μm for the IRS/Spitzer spectra (see Table 2). An upper limit for the flux of the PAH is listed for those objects in which the feature is not clearly detected above the underlying continuum within the uncertainties. Shi et al. (2007) uses two Drude profiles centered at 11.23 and 11.33 μm, with a fixed FWHM and the slope of the underlying silicate profile as the continuum, to measure the PAH on a sample of PG QSOs that includes most of the objects in our sample. The fluxes we measure for the PAH feature at 11.3 μm are comparable to those reported by Shi et al. (2014; see the left panel of Figure 3).

3.2. The Stacked Inner and Larger Aperture Nuclear Spectrum

The limited S/N in the CC and VISIR spectra make the detection of the PAH at 11.3 μm in individual spectra difficult. We separate the 13 QSOs with CC and VISIR spectra into two groups according to the inner physical scale (<0.7 kpc and 0.7 to 1 kpc) probed by the slit-widths (see Table 1). This allows us to combine similar spatial scales and to keep track of the spatial resolution into the subsequent analysis, and stack the rest-frame high angular resolution spectra of each group in order to improve the S/N (see Table 3 and Figure 2). The stacking was done combining the normalized spectra at 10 μm of each QSO assuming an equally weighted average (see Figure 2). We multiply the final resulting stacked spectra by their corresponding average flux at 10 μm. The final error is estimated as the error propagation of the rms uncertainty. We measure the S/N using the same continuum bands as with the individual CC and VISIR spectra. For the stacked spectrum of group 2, we obtain an S/N = 6 that is nearly twice better than the average S/N of the group. For the stacked spectrum of group 1 we estimate a similar S/N than the average S/N of the group.

Note that group 1 includes a QSO that has an angular resolution corresponding to 376 pc, which is nearly two times better than the average resolution of other QSOs in the group (see Tables 1 and 3 and and Figure 2). The result that we obtain without considering this object is the same within the uncertainties. We also stacked the spectra of all 13 QSOs and estimate the flux of the PAH (see Table 3 and Figure 2). However, this result should be used and interpreted carefully because we are combing different physical scales that range from $\sim$300 to 1 kpc.

PG 1440+356 (MRK 478) is the only QSO exhibiting strong 11.3 μm PAH emission (EW$_{11.3\ \mu m} \sim 0.04\ \mu$m) allowing a clear detection of this feature in the CC/GTC spectrum with an S/N = 8. We note that removing this object from group 2 gives a similar flux and the PAH is still detected. Errors in the spectra (see Figure 1) include only the rms uncertainty, but typical errors of nearly 10% to 15% associated with the photometric calibration at N-band should also be considered (see, Alonso-Herrero et al. 2016a; Martínez-Paredes et al. 2017).

In order to make a proper comparison between the results obtained from the PAH at 11.3 μm on the CC and VISIR stacked spectra and the IRS/Spitzer spectra, we stacked the IRS/Spitzer spectra of each group and followed the same methodology described in Section 3.2 to measure the flux and EW of the PAH at 11.3 μm (see Table 3).
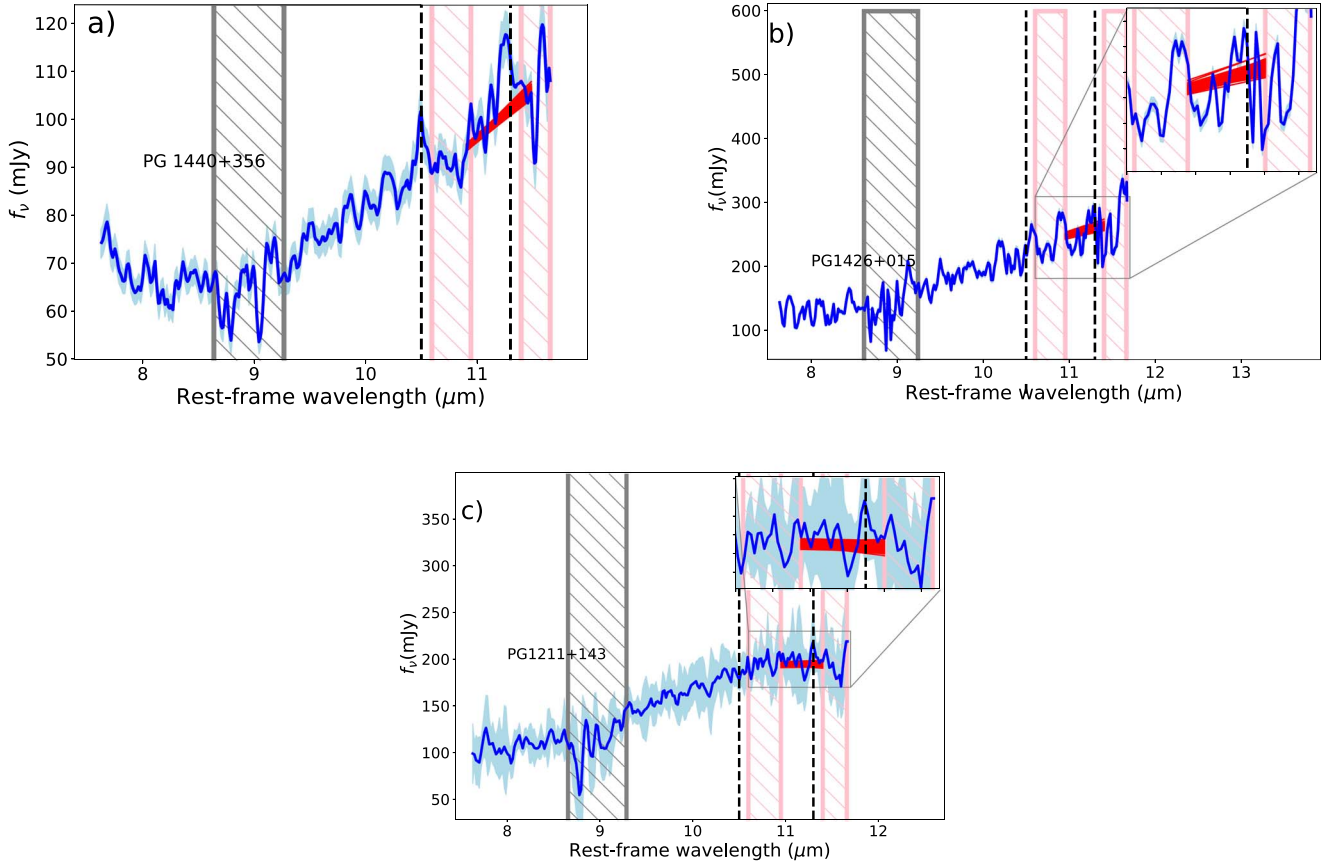
Figure 1. CC spectra of PG 1440+356 (MRK 478, panel (a)), PG 1426+015 (panel (b)), and PG 1211+143 (panel (c)). The solid red lines are local continua generated through Monte Carlo simulations. The vertical dashed lines indicate the position of the PAH at 11.3 μm and of the [S IV]10.5 μm emission. The two hatched pink regions represent the bands used to measure the continua. The gray hatched region marks the approximate spectral range of low atmospheric transmission.

Table 2
Inner (CC and VISIR) and Larger (*Spitzer*) Aperture Flux and EW of the PAH at 11.3 μm, Plus the SFR and BH Accretion Rate

Name	Inner Aperture			Larger Aperture			
	$f_{11.3\ \mu m}$ 10^{-13} erg s^{-1} cm^{-2}	EW$_{11.3\ \mu m}$ μm	SFR$_{IRS}$ $M_\odot$ yr^{-1}	$f_{11.3\ \mu m}$ 10^{-13} erg s^{-1} cm^{-2}	EW$_{11.3\ \mu m}$ μm	SFR$_{inner}$ $M_\odot$ yr^{-1}	$\dot{M}_{BH}$ $M_\odot$ yr^{-1}
PG 1501+106	<0.23	<0.057	<0.2	<0.3	<0.007	<0.2	0.1
MRK 509	1.15 ± 0.07	0.014 ± 0.001	0.7 ± 0.2[a]	2.65 ± 0.01	0.0401 ± 0.0001	1.7 ± 0.5	1.1
PG 2130+099	0.38 ± 0.04	0.028 ± 0.002	0.8 ± 0.3	0.45 ± 0.02	0.0105 ± 0.0004	1.0 ± 0.3	0.04
PG 1229+204	<0.3	<0.02	<0.6	<0.2	<0.02	<0.5	0.04
PG 0844+349	<0.2	<0.01	<0.4	<0.2	<0.02	<0.5	0.1
MR 2251−178	<0.54	<0.03	<1.6	...	...	...	0.6
PG 0003+199	0.48 ± 0.05	0.022 ± 0.003	0.15 ± 0.05	0.493 ± 0.005	0.0109 ± 0.0001	0.15 ± 0.05	0.002
PG 1440+356	0.83 ± 0.07	0.035 ± 0.003	3 ± 1	1.607 ± 0.008	0.0739 ± 0.0004	6 ± 2	0.1
PG 1211+143	<0.4	<0.02	<1.5	<0.3	<0.008	<1.2	0.1
PG 1426+015	0.43 ± 0.06	0.0072 ± 0.0001	1.9 ± 0.6	0.38 ± 0.02	<0.03	<1.7	0.2
PG 1411+442	<0.2	<0.01	<0.9	<0.3	<0.01	<1.5	0.03
PG 0050+124	<0.6	<0.006	<1	1.47 ± 0.05	0.0132 ± 0.0004	3 ± 1	0.1
PG 0804+761	<0.2	<0.01	<1.2	<0.2	<0.005	<1.1	0.6
PG 1448+273	...	...	...	0.480 ± 0.008	0.0400 ± 0.0007	1.1 ± 0.4	0.03
PG 1534+580	...	...	...	0.35 ± 0.01	0.0166 ± 0.0005	0.14 ± 0.05	0.02
PG 1535+547	...	...	...	0.32 ± 0.05	0.023 ± 0.003	0.24 ± 0.08	0.004
PG 2214+139	...	...	...	<0.2	<0.01	<0.5	0.10
PG 0923+129	...	...	...	1.27 ± 0.01	0.0470 ± 0.0005	0.6 ± 0.2	0.03
PG 1351+640	...	...	...	1.47 ± 0.03	0.0321 ± 0.0006	7.3 ± 2.3	0.01
PG 0007+106	...	...	...	0.44 ± 0.02	0.025 ± 0.001	2.1 ± 0.7	0.2

Notes. Column 1 gives the name, columns 2, 3, and 4 give the inner aperture flux, EW, and SFR, while columns 5, 6 and 7 give the larger aperture flux, EW, and SFR. Column 8 lists the BH accretion rates.
[a] Similar value was reported by Esquej et al. (2014).

Table 3
Flux and EW of the PAH at 11.3 μm from the Inner (CC and VISIR) and Larger Aperture (IRS/Spitzer) Stacked Spectra

| Name | Inner Aperture | | | Larger Aperture | | |
| | Physical Scale | $f_{11.3\,\mu m}$ | EW$_{11.3\,\mu m}$ | Physical Scale | $f_{11.3\,\mu m}$ | EW$_{11.3\,\mu m}$ |
	kpc	10^{-13} erg s^{-1} cm^{-2}	μm	kpc	10^{-13} erg s^{-1} cm^{-2}	μm
Group 1 (seven QSOs)	<0.7	<0.2	<0.006	3.1	0.56 ± 0.01	0.0151 ± 0.0003
Group 2 (six QSOs)	0.7–1	0.72 ± 0.03	0.015 ± 0.001	5.2	0.94 ± 0.02	0.0214 ± 0.0004
All (13 QSOs)	<1	<0.09	<0.01	4.1	0.73 ± 0.01	0.0179 ± 0.0003

Note. Column 1 lists the group. Column 2 lists the average physical scale of the inner spectra. Columns 3 and 4 give the inner (CC and VISIR) flux and EW. Column 5 gives the average physical scale of the larger *Spitzer* aperture, while columns 6 and 7 give the larger aperture flux and EW.
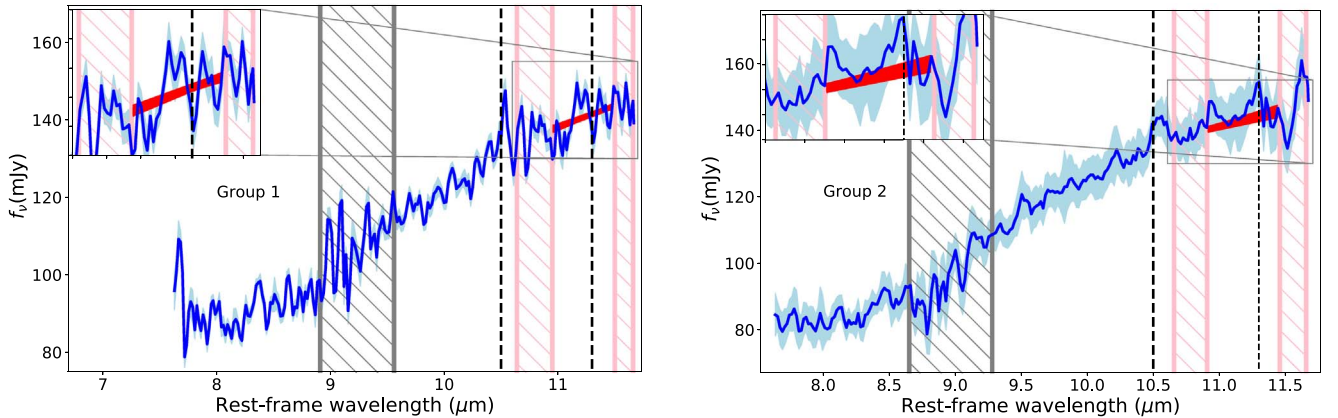
Figure 2. Stacked rest-frame high angular resolution spectra. Left: stacked spectrum of group 1 (physical scale <0.7 kpc). Right: stacked spectrum of group 2 (physical scale <1 kpc). The solid red lines are the local continua generated through Monte Carlo simulations. The vertical dashed black lines indicate the position of the PAH at 11.3 μm and of the [S IV] 10.5 μm emission. The two hatched pink regions show the bands used to measure the continua. The gray hatched region marks the approximate spectral range of low atmospheric transmission.

4. Star Formation Rates

Shipley et al. (2016) calibrated the integrated luminosity of PAHs at 6.2, 7.7, and 11.3 μm as a function of the SFR using the IRS/*Spitzer* observations of a sample of 105 galaxies with IR luminosities between 10^9 and $10^{12}\,L_\odot$. They used the extinction-corrected H_α to derive the SFRs. For these calculations a Kroupa initial mass function with a slope $\alpha = 2.3$ for stellar masses 0.5–100 $M_\odot$ and a shallower slope $\alpha = 1.3$ for the mass range 0.1–0.5 $M_\odot$ was assumed (Kroupa & Weidner 2003). We calculate the SFR using their linear relationship:

$$\log \text{SFR}(M_\odot \text{ yr}^{-1}) = (-44.14 \pm 0.08) + (1.06 \pm 0.03)$$
$$\times \log L_{11.3\,\mu m} \text{ (erg s}^{-1}). \qquad (1)$$

In Table 2 we report the SFRs derived from the IRS/*Spitzer* spectra. Shipley et al. (2016) found that a difference of a factor of two can be obtained in the SFRs derived from PAHs, according to the method used to estimate them.

Shi et al. (2014) estimated the SFRs for most QSOs in our sample using the star-forming templates from Rieke et al. (2009). However, they point out that an issue with this method is the large intrinsic scatter between PAH fluxes and SFRs, which results from the way they anchor the continuum (Calzetti et al. 2007; Smith et al. 2007). In Figure 3 we compare the SFRs derived in this work with those derived by Shi et al. (2014). We observe that their SFRs are shifted to larger values. We find that the SFRs derived by Shi et al. (2014) are on average three times larger than the SFRs we derive from the PAH at 11.3 μm using Equation (1). However, we note that if

we use the PAH measurements by the Shi et al. (2007) and the Shipley et al. (2016) relationship (Equation (1)), the SFRs are similar to those derived by us (see Table 2).

4.1. Star Formation in the Central Few Hundred Parsecs

Previous works attributed the origin of PAH features in the IRS/*Spitzer* spectra of local QSOs to star-forming regions in the host galaxy on scales of a few kiloparsecs (e.g., Shi et al. 2007; Schweitzer et al. 2008; Shi et al. 2014). However, high angular resolution observations of local Seyferts have shown that the PAH at 11.3 μm can be detected at scales of a few parsecs and hundreds of parsecs (Esquej et al. 2014), supporting the idea that this feature can survive the strong nuclear radiation of the AGN (Hönig et al. 2010; Diamond-Stanic & Rieke 2012; Alonso-Herrero et al. 2014).

The inner (∼few hundred parsecs) MIR emission of QSOs is mostly dominated by an unresolved component associated with the dusty torus (Martínez-Paredes et al. 2017). However, the emission of PAH at 11.3 μm is clearly present in the high angular resolution spectrum of five QSOs, and in the stacked spectra of group 2 on scales of ∼1 kpc. Indeed, the emission of the PAH at 11.3 μm is strong (S/N = 8) in the high angular resolution spectrum of PG 1440+356 (MRK 478) on scales of ∼0.7 kpc.

We estimate the inner-aperture (CC and VISIR) SFR of the 13 QSOs in our sample with high angular resolution spectra (see Table 2), the SFR of the stacked spectra of groups 1 and 2, and of the stack of all QSOs (see Table 4). Note that PG 1440 +356 (MRK 478) is one of the objects in group 2. Removing
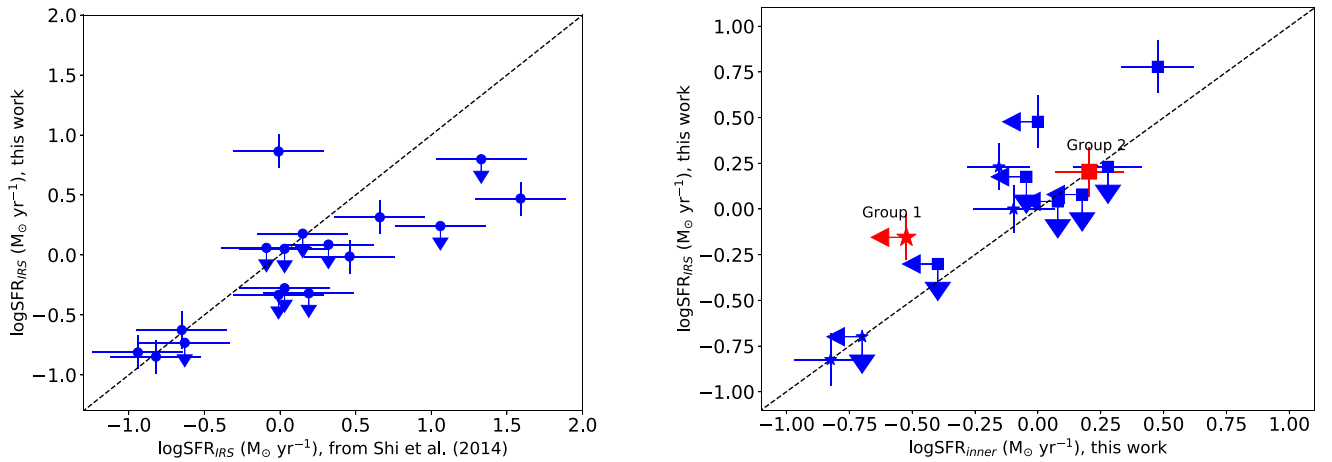
Figure 3. Left: comparison between the larger aperture (IRS/*Spitzer*) SFR$_{IRS}$ estimated by Shi et al. (2014) and in this work. Right: comparison between the larger aperture (IRS/*Spitzer*) SFR$_{IRS}$ and the inner SFR$_{inner}$ estimated in this work. The red star and square mark the values measured for the stacked spectra of groups 1 and 2.

Table 4
Inner (CC/VISIR) and Larger Aperture (IRS/*Spitzer*) Star Formation Rates

Name or Group	SFR$_{inner}$ $M_\odot\ \mathrm{yr}^{-1}$	SFR$_{IRS}$ $M_\odot\ \mathrm{yr}^{-1}$
Group 1 (seven-QSOs)	<0.3	0.7 ± 0.2[a]
Group 2 (six-QSOs)	1.6 ± 0.5	1.6 ± 0.5
All (13-QSOs)	<0.2	1.8 ± 0.5

Notes. Column 1 lists the group, columns 2 and 3 give the inner and larger aperture SFRs.
[a] The SFR$_{IRS}$ of group 1 is calculated with the stacked spectra of six objects, because MR 2251−178 does not have IRS/*Spitzer* spectrum.

this QSO from group 2 does not change our estimation of the SFR within the uncertainties.

Using the same PAH and technique, we calculate the larger aperture SFRs from the IRS/*Spitzer* spectrum of each QSO and from the stacked spectra of groups 1 and 2. Comparing the inner (few hundred parsec) and larger aperture (few kiloparsec) SFRs we find that they are similar (see the right panel in Figure 3). Therefore, it is likely that the star formation activity detected on larger scales is mainly concentrated within the central kiloparsec. Additionally, we find that at least half of the SFR estimated from the IRS/*Spitzer* spectrum of PG 1440 +356 (MRK 478) arises from an inner region of ∼0.7 kpc (see Figures 1 and 4). These results suggest that the circumnuclear SFR in local MIR-bright QSOs is more centrally peaked than previously assumed, and they give evidence on the survival of the PAH at 11.3 μm near the strong radiation field of the AGN, on scales of few hundreds of parsecs.

5. The Role of AGN Activity on the Inner Star Formation

During the last decades, AGN and star formation activity have been widely studied by several authors (e.g., Nicholson et al. 1998; Best et al. 2005; Schawinski et al. 2007; Rafanelli et al. 2011; Fabian 2012; Diniz et al. 2015; Baron et al. 2017). Despite the great effort, however, the way in which AGN activity influences the gas in the host galaxy, among the various classes, sizes, and luminosities of AGNs, is still uncertain (Beckmann & Shrader 2012).

Hopkins & Quataert (2010) presented multiscale smoothed particle hydrodynamic simulations of gravitational torques and

gas inflow in AGNs from kiloparsec to subparsec scales, reaching a region where the material becomes a standard thin accretion disk. The simulations included as main ingredients: gas, stars, BHs, self-gravity, star formation, and stellar feedback. BH feedback was not included in order to isolate the physics of angular momentum transport. These simulations predict correlations between the BH accretion rate and the SFR at different physical scales from the central black hole. Their simulations suggest that nuclear star formation (<10 pc) is strongly coupled to AGN activity, following a linear relation (1:1) between BH accretion rate and SFR, while for scales <100 pc, <1 kpc, and <50 kpc scales the relationship changes by a factor of 10, 100, and 1000, respectively.

The AGN bolometric luminosity is estimated using the relation derived by Marconi et al. (2004),

$$L_{\mathrm{bol}} = kL(2\text{–}10\ \mathrm{keV}), \qquad (2)$$

where k is a bolometric correction factor that depends on the hard X-ray luminosity (2–10 keV) as a three-order polynomial, $\log(L/L(2\text{–}10\ \mathrm{keV})) = 1.54 + 0.24\mathcal{L} + 0.012\mathcal{L}^2 - 0.0015\mathcal{L}^3$, where $\mathcal{L} = \log(L_{\mathrm{bol}}/L_\odot) - 12$. Then, we calculate the BH accretion rate using the relation obtained by Alexander & Hickox (2012),

$$\dot{M}_{\mathrm{BH}}(M_\odot\ \mathrm{yr}^{-1}) = 0.15\frac{0.1}{\epsilon}\frac{L_{\mathrm{bol}}}{10^{45}}, \qquad (3)$$

where $\epsilon = 0.1$ is the typical value for the mass-energy conversion efficiency in the local universe (Marconi et al. 2004). In Table 2 we list the BH accretion rates derived from Equation (3).

In Figure 4 we plot the BH accretion rate against the larger aperture SFR measured in the individual IRS/*Spitzer* spectra of our QSOs, on scales from 1 to 6 kpc, and the inner (CC and VISIR) SFRs measured in the stacked spectra of groups 1 and 2, on scales of <0.7 kpc and ∼0.7 to 1 kpc, respectively. We compare our measurements with merger simulations of Hopkins & Quataert (2010), and note that ∼58% of the objects in our sample lies on the valid lower BH accretion rates and SFRs of the model. We note that larger aperture SFRs measured on scales of ∼3 kpc for group 1 (stars) and ∼5 kpc for group 2 (squares) are lower than the median SFRs predicted by simulations, on the same scales and assuming a linear
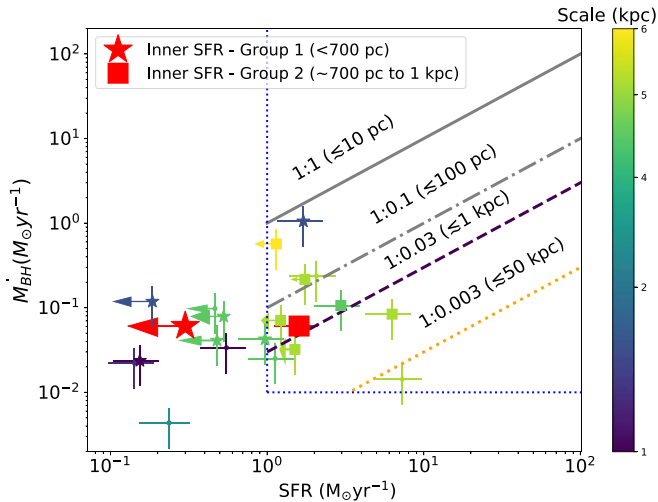
Figure 4. BH accretion rate as a function of the larger aperture (IRS/*Spitzer*) SFR of QSOs, as derived from Equation (1). The points follow the color code of the vertical bar, which indicates the central physical regions where the SFR is measured. These range from 1 to 6 kpc. The stars represent objects in group 1, while squares represent objects in group 2. The red star and square represent the inner SFR measured on the CC and VISIR stacked spectra of groups 1 and 2, respectively. The uncertainty on the BH accretion rate is assumed to be 50% due to the large hard X-ray variability of the flux in these objects (e.g., Soldi et al. 2014). The solid gray line is the 1:1 SFR: $\dot{M}_{BH}$ applicable to scales $\lesssim$10 pc, the dashed–dotted gray line is the 1:0.1 ($\lesssim$100 pc) ratio, the dashed dark purple line is the 1:0.03 ($\lesssim$1 kpc) ratio, and the dotted orange line is the 1:0.003 relation (see the text and Hopkins & Quataert 2010). The upper-right section enclosed by the dotted blue lines represents the limits above which the model is physically valid (see the text and Hopkins & Quataert 2010).

proportionality. A similar result was found by Ho (2005) using the [O II]λ3727 emission line to estimate the SFRs on similar scales for a sample of PG QSOs ($z < 0.3$). Hopkins & Quataert (2010) argued that because QSOs are on the tail of the BH accretion rate and SFR distributions, it is plausible that the AGN feedback-dominated evolutionary stage is not well accounted for in their simulations. This is especially relevant for group 1, which has an average redshift of $z = 0.05$ that is 1.6 times lower than the average redshift of group 2. Therefore, we conclude that the extrapolation of the simulations is overpredicting the SFRs at the physical scales we probe for these bright nearby QSOs.

On the other hand, the low SFRs ($<0.5\,M_\odot\,\mathrm{yr}^{-1}$) measured in most QSOs of group 1 at scales of 0.7 kpc to 1 kpc (see the right panel of Figure 3), or at larger apertures $\sim$3 kpc (as the data in the lower left corner of Figure 4), indicates that these objects are not hosted in galaxies with strong starbursts. Ho (2005) did not detect the on-going star formation in QSO hosts using his [O II]λ3727 diagnosis on galactic scales either. Considering that many of these galaxies contain significant reservoirs of molecular gas (Ho 2005; Xia et al. 2012; Shangguan et al. 2018), the star formation efficiency in the host of QSO could be quenched. A high spatial resolution millimeter/submillimeter interferometer could confirm this scenario.

Another possibility is that PAH in QSOs is not effectively tracing the star formation within a few kiloparsecs (see, e.g., Voit 1992; Sales et al. 2010, and references therein). However, we note that for nine objects in our sample the optical SFRs (upper limits) derived by Ho (2005) are similar to the larger aperture PAHs–SFRs reported by us. While, the FIR–SFR derived by Petric et al. (2015) for a sample of 31 local (<0.5
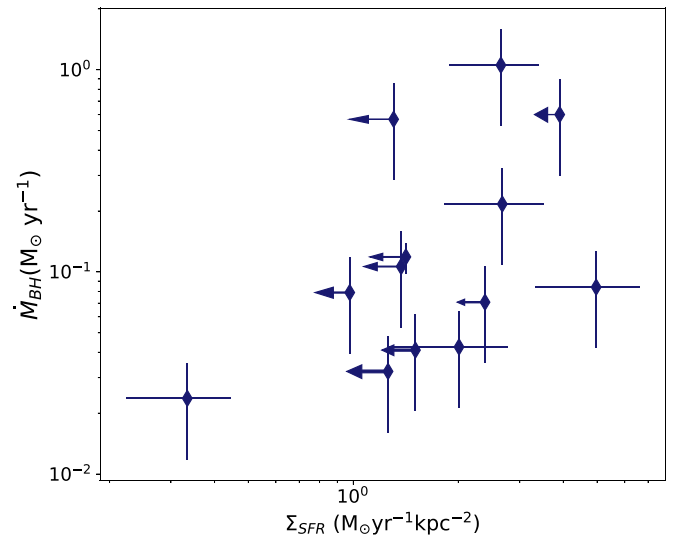

Figure 5. BH accretion rate as a function of the SFR density.

QSOs, that include the most objects in our sample, are larger. It is important to note that their FIR–SFRs are measured on even larger apertures ($\sim$20 arcsec, corresponding to several kiloparsecs) and that a fraction of the FIR emission could be heated by other sources like old stars (e.g., Symeonidis et al. 2016; Shangguan et al. 2018).

For group 2 we find that the inner SFR measured in the high angular resolution stacked spectrum on scales $\lesssim$1 kpc is in agreement with the 1:0.03 SFR: $\dot{M}_{BH}$ applicable to scales of $\lesssim$1 kpc. These results are consistent with a scenario in which the star formation activity in these QSOs is the same within the first 5 kpc from the central engine and is more centrally concentrated on the first kiloparsec.

Finally, we use our estimates of the inner SFR between $\sim$0.3 and 1 kpc to derive the SFR density (Σ_{SFR}), which is expected to be related to the nuclear molecular gas density of the host galaxy (Schmidt 1959; Kennicutt 1989, 1998; Kennicutt & Evans 2012). In Figure 5 we plot the BH accretion rate as a function of the SFR density. However, due to the large errors of the BH accretion rates and the narrow range in hard X-ray luminosity ($\sim$10^{43}–10^{44} erg s^{-1}) covered by our sample, it is difficult to identify any reliable correlation. Therefore, future comparisons should include objects with lower and higher hard X-ray luminosities compared to those covered by our work. These comparisons will be useful for future spatially resolved studies of the Kennicutt–Schmidt law in quasar hosts.

More sensitive data, such as those that will be obtained with the Midinfrared Instrument (MIRI) on board the *James Webb Space Telescope* (*JWST*) and higher angular resolution data to be obtained with the MIR instrument on 20–40 m class telescopes, will be necessary to better constrain the location of the nuclear (few parsecs) and circumnuclear (few kiloparsecs) starbursts responsible for this emission, and consequently to test updated models. On the other hand, measurements of the molecular gas in nearby QSOs, such as those obtained with NOEMA and ALMA, would allow the investigation of the possible correlation between inner star formation and AGN activity, because the large molecular mass detected in PG 1440+356 (MRK 478) (Rodríguez-Ardila & Viegas 2003), IZw1 (Evans et al. 2001), and in most QSOs (e.g., Evans et al. 2001, 2006; Scoville et al. 2003; Bertram et al. 2007; Krips et al. 2012; Xia et al. 2012; Villar-Martín et al. 2013; Rodríguez et al. 2014) could be protecting the surviving PAH

molecules from the strong AGN radiation, as suggested by Esquej et al. ([2014](#)) and Alonso-Herrero et al. ([2014](#)) for Seyfert galaxies.

6. Summary and Conclusions

We use a sample of 20 nearby QSOs ($z < 0.1$) with both IRS/*Spitzer* (19/20) and high angular resolution (13/20) MIR spectra in order to measure the 11.3 μm PAH emission and EW on scales of a few kiloparsecs and hundreds of parsecs.

We detect clear 11.3 μm PAH emission in 58% of QSOs with IRS/*Spitzer* spectra, while we estimate an upper limit for the rest. We find clear emission of the PAH at 11.3 μm in five QSOs with CC and VISIR spectra, while we measure an upper limit in the other eight. Additionally, we build two groups according to their physical scale probed by the slit-width (<1 arcsec) of the high angular resolution spectra. This allows us to combine spectra obtained on similar physical scales and to improve the S/N. For group 1 we measure the PAH at 11.3 μm on the stacked spectrum within an inner region of <0.7 kpc, while for group 2 we measure the PAH on the stacked spectrum within an inner region of ~0.7–1 kpc. In order to make a consistent comparison, we also stacked the IRS/*Spitzer* spectra of group 1 and 2, and measured the PAHs on scales of ~3 and ~5 kpc.

Using the same technique and the luminosity of the PAH at 11.3 μm we estimate larger (few kiloparsecs) and inner (few hundred paresecs) aperture SFRs. We calculate the larger aperture SFRs for 19 QSOs with IRS/*Spitzer* spectra, and the inner aperture SFRs for 13 objects with high angular resolution spectra. Additionally, we calculate the larger and inner aperture SFRs for groups 1 and 2 with IRS/*Spitzer* as well as CC and VISR stacked spectra.

We compare the inner and larger aperture SFRs of each group and find that they are similar. We conclude that star formation activity is present in the most nearby MIR-bright QSOs at scales of a few hundred parsecs. Finally, we calculate both the star formation and black hole accretion rate and compare them with merger simulations. We find that QSOs in group 2 show centrally concentrated star formation activity on scales $\lesssim 1$ kpc in agreement with simulations. Additionally, we note that the SFRs measured on few kiloparsec scales are lower than those predicted by simulations. However, because QSOs are on the tail of the BH accretion rate and SFR distributions, it is possible that the evolutionary stage of objects in group 1, which have an average redshift 1.6 times lower than the average redshift of group 2 ($z = 0.08$), is not well suited to these simulations. However, it is also possible that the star formation efficiency in the host galaxy is being quenched beyond the predictions of the models, and/or that the SFR derived from PAH at 11.3 μm is not tracing the star formation activity well due to the destruction or dilution of PAH by the strong radiation of the AGN.

In any case, future higher angular resolution and more sensitive data as those expected from the MIR instruments on 20–40 m class telescopes and the MIRI on board the *JWST* will allow us to constrain these scenarios in a better way.

Finally, we use the inner SFR and physical scale to estimate the SFR density and compare it with the BH accretion rates. We do not find any reliable correlation. Future studies should include lower and higher hard X-ray luminosities than the ones presented here. This could help interpret future observations of the nuclear molecular gas in local QSOs.

ORCID iDs

M. Martínez-Paredes ⓘ https://orcid.org/0000-0002-0088-0103
I. Aretxaga ⓘ https://orcid.org/0000-0002-6590-3994

References

Alexander, D. M., & Hickox, R. C. 2012, NewAR, 56, 93
Alonso-Herrero, A., Esquej, P., Roche, P. F., et al. 2016a, MNRAS, 455, 563
Alonso-Herrero, A., Poulton, R., Roche, P. F., et al. 2016b, MNRAS, 463, 2405
Alonso-Herrero, A., Ramos Almeida, C., Esquej, P., et al. 2014, MNRAS, 443, 2766
Azadi, M., Aird, J., Coil, A. L., et al. 2015, ApJ, 806, 187
Ballantyne, D. R. 2008, ApJ, 685, 787
Baron, D., Netzer, H., Poznanski, D., Prochaska, J. X., & Förster Schreiber, N. M. 2017, MNRAS, 470, 1687
Beckmann, V., & Shrader, C. 2012, in Proc. "An INTEGRAL View of the High-energy Sky (the first 10 years)"—9th INTEGRAL Workshop and Celebration of the 10th Anniversary of the Launch (Trieste: PoS), 69
Bertram, T., Eckart, A., Fischer, S., et al. 2007, A&A, 470, 571
Best, P. N., Kauffmann, G., Heckman, T. M., et al. 2005, MNRAS, 362, 25
Burtscher, L., Meisenheimer, K., Tristram, K. R. W., et al. 2013, A&A, 558, AA149
Calzetti, D., Kennicutt, R. C., Engelbracht, C. W., et al. 2007, ApJ, 666, 870
Cid Fernandes, R., Jr., & Terlevich, R. 1995, MNRAS, 272, 423
Colina, L., Vargas, M. L. G., Delgado, R. M. G., et al. 1997, ApJL, 488, L71
Cresci, G., Maiolino, R., Marconi, A., Mannucci, F., & Granato, G. L. 2004, A&A, 423, L13
Davies, R. I., Müller Sánchez, F., Genzel, R., et al. 2007, ApJ, 671, 1388
Delvecchio, I., Lutz, D., Berta, S., et al. 2015, MNRAS, 449, 373
Deo, R. P., Crenshaw, D. M., & Kraemer, S. B. 2006, AJ, 132, 321
Diamond-Stanic, A. M., & Rieke, G. H. 2010, ApJ, 724, 140
Diamond-Stanic, A. M., & Rieke, G. H. 2012, ApJ, 746, 168
Diniz, M. R., Riffel, R. A., Storchi-Bergmann, T., & Winge, C. 2015, MNRAS, 453, 1727
Dong, X. Y., & Wu, X.-B. 2016, ApJ, 824, 70
Du, P., Hu, C., Lu, K.-X., et al. 2015, ApJ, 806, 22
Esparza-Arredondo, D., González-Martín, O., Dultzin, D., et al. 2018, ApJ, 859, 124
Esquej, P., Alonso-Herrero, A., González-Martín, O., et al. 2014, ApJ, 780, 86
Evans, A. S., Frayer, D. T., Surace, J. A., & Sanders, D. B. 2001, AJ, 121, 1893
Evans, A. S., Solomon, P. M., Tacconi, L. J., Vavilkin, T., & Downes, D. 2006, AJ, 132, 2398

Fabian, A. C. 2012, ARA&A, 50, 455
Farrah, D., Bernard-Salas, J., Spoon, H. W. W., et al. 2007, ApJ, 667, 149
Feruglio, C., Maiolino, R., Piconcelli, E., et al. 2010, A&A, 518, L155
González Delgado, R. M., Heckman, T., Leitherer, C., et al. 1998, ApJ, 505, 174
González-Martín, O., Rodríguez-Espinosa, J. M., Díaz-Santos, T., et al. 2013, A&A, 553, AA35
Gültekin, K., Cackett, E. M., Miller, J. M., et al. 2009, ApJ, 706, 404
Gürkan, G., Hardcastle, M. J., Jarvis, M. J., et al. 2015, MNRAS, 452, 3776
Heckman, T. M., González-Delgado, R., Leitherer, C., et al. 1997, ApJ, 482, 114
Hernán-Caballero, A., & Hatziminaoglou, E. 2011, MNRAS, 414, 500
Ho, L. C. 2005, ApJ, 629, 680
Hönig, S. F., Kishimoto, M., Gandhi, P., et al. 2010, A&A, 515, AA23
Hopkins, P. F., & Quataert, E. 2010, MNRAS, 407, 1529
Houck, J. R., & Roellig, T. L., Van Cleve, J., et al. 2004, Proc. SPIE, 5487, 62
Imanishi, M., & Wada, K. 2004, ApJ, 617, 214
Jensen, J. J., Hönig, S. F., Rakshit, S., et al. 2017, MNRAS, 470, 3071
Kennicutt, R. C., & Evans, N. J. 2012, ARA&A, 50, 531
Kennicutt, R. C., Jr. 1989, ApJ, 344, 685
Kennicutt, R. C., Jr. 1998, ApJ, 498, 541
Krips, M., Neri, R., & Cox, P. 2012, ApJ, 753, 135
Kroupa, P., & Weidner, C. 2003, ApJ, 598, 1076
Lebouteiller, V., Barry, D. J., Spoon, H. W. W., et al. 2011, ApJS, 196, 8
Magorrian, J., Tremaine, S., Richstone, D., et al. 1998, AJ, 115, 2285
Marconi, A., Risaliti, G., Gilli, R., et al. 2004, MNRAS, 351, 169
Martínez-Paredes, M., Aretxaga, I., Alonso-Herrero, A., et al. 2017, MNRAS, 468, 2
Mason, R. E., Levenson, N. A., Packham, C., et al. 2007, ApJ, 659, 241
Matsuoka, K., & Woo, J.-H. 2015, ApJ, 807, 28
Miller, J. M., Kaastra, J. S., Miller, M. C., et al. 2015, Natur, 526, 542
Mullaney, J. R., Alexander, D. M., Goulding, A. D., & Hickox, R. C. 2011, MNRAS, 414, 1082
Netzer, H. 2009, ApJ, 695, 793
Netzer, H., Lutz, D., Schweitzer, M., et al. 2007, ApJ, 666, 806
Nicholson, K. L., Reichert, G. A., Mason, K. O., et al. 1998, MNRAS, 300, 893
Oliva, E., Origlia, L., Kotilainen, J. K., & Moorwood, A. F. M. 1995, A&A, 301, 55
Packham, C., Telesco, C. M., Hough, J. H., & Ftaclas, C. 2005, RMxAC, 24, 7
Peeters, E., Hony, S., Van Kerckhoven, C., et al. 2002, A&A, 390, 1089
Peterson, B. M., & Wandel, A. 2000, ApJL, 540, L13
Petric, A. O., Ho, L. C., Flagey, N. J. M., & Scoville, N. Z. 2015, ApJS, 219, 22
Pope, A., Chary, R.-R., Alexander, D. M., et al. 2008, ApJ, 675, 1171
Pović, M., Márquez, I., Netzer, H., et al. 2016, MNRAS, 462, 2878
Rafanelli, P., La Mura, G., Bindoni, D., et al. 2011, BaltA, 20, 419
Ramos Almeida, C., Alonso-Herrero, A., Esquej, P., et al. 2014, MNRAS, 445, 1130
Rieke, G. H., Alonso-Herrero, A., Weiner, B. J., et al. 2009, ApJ, 692, 556
Roche, P. F., Packham, C., Telesco, C. M., et al. 2006, MNRAS, 367, 1689
Rodríguez-Ardila, A., & Viegas, S. M. 2003, MNRAS, 340, L33
Rodríguez, M. I., Villar-Martín, M., Emonts, B., et al. 2014, A&A, 565, A19
Rosario, D. J., Santini, P., Lutz, D., et al. 2012, A&A, 545, A45
Ruschel-Dutra, D., Rodríguez Espinosa, J. M., González Martín, O., Pastoriza, M., & Riffel, R. 2017, MNRAS, 466, 3353
Sales, D. A., Pastoriza, M. G., & Riffel, R. 2010, ApJ, 725, 605
Schawinski, K., Thomas, D., Sarzi, M., et al. 2007, MNRAS, 382, 1415
Schmidt, M. 1959, ApJ, 129, 243
Schweitzer, M., Groves, B., Netzer, H., et al. 2008, ApJ, 679, 101
Schweitzer, M., Lutz, D., Sturm, E., et al. 2006, ApJ, 649, 79
Scoville, N. Z., Frayer, D. T., Schinnerer, E., & Christopher, M. 2003, ApJL, 585, L105
Shangguan, J., Ho, L. C., & Xie, Y. 2018, ApJ, 854, 158
Shi, Y., Ogle, P., Rieke, G. H., et al. 2007, ApJ, 669, 841S
Shi, Y., Rieke, G. H., Ogle, P. M., Su, K. Y. L., & Balog, Z. 2014, ApJS, 214, 23
Shimizu, T. T., Mushotzky, R. F., Meléndez, M., Koss, M., & Rosario, D. J. 2015, MNRAS, 452, 1841
Shipley, H. V., Papovich, C., Rieke, G. H., Brown, M. J. I., & Moustakas, J. 2016, ApJ, 818, 60
Smith, J. D. T., Draine, B. T., Dale, D. A., et al. 2007, ApJ, 656, 770
Soldi, S., Beckmann, V., Baumgartner, W. H., et al. 2014, A&A, 563, A57
Stanley, F., Harrison, C. M., Alexander, D. M., et al. 2015, MNRAS, 453, 591
Symeonidis, M., Giblin, B. M., Page, M. J., et al. 2016, MNRAS, 459, 257
Terlevich, E., Díaz, A. I., & Terlevich, R. 1990, RMxAA, 21, 218
Terlevich, E., Terlevich, R., & Liaz, A. 1992, in ASP Conf. Ser. 31, Relationships Between Active Galactic Nuclei and Starburst Galaxies, ed. A. V. Filippenko (San Francisco, CA: ASP), 231
Thompson, T. A., Quataert, E., & Murray, N. 2005, ApJ, 630, 167
Treyer, M., Schiminovich, D., Johnson, B. D., et al. 2010, ApJ, 719, 1191
Uchida, K. I., Sellgren, K., Werner, M. W., & Houdashelt, M. L. 2000, ApJ, 530, 817
Villar-Martín, M., Rodríguez, M., Drouart, G., et al. 2013, MNRAS, 434, 978
Voit, G. M. 1992, in ASP Conf. Ser. 31, Relationships Between Active Galactic Nuclei and Starburst Galaxies, ed. A. V. Filippenko (San Francisco, CA: ASP), 87
Wada, K., & Norman, C. A. 2002, ApJL, 566, L21
Watabe, Y., Kawakatu, N., & Imanishi, M. 2008, ApJ, 677, 895
Werner, M. W., Roellig, T. L., Low, F. J., et al. 2004, ApJS, 154, 1
Xia, X. Y., Gao, Y., Hao, C.-N., et al. 2012, ApJ, 750, 92
Xie, Y., Ho, L. C., Li, A., & Shangguan, J. 2018, ApJ, 860, 154
Zhou, X.-L., & Zhang, S.-N. 2010, ApJL, 713, L11